ELSEVIER

Chemical Physics 266 (2001) 285–294

Chemical Physics

www.elsevier.nl/locate/chemphys

Vibrational-exciton relaxation probed by three-pulse echoes in polypeptides

Andrei Piryatinski [1], Vladimir Chernyak [2], Shaul Mukamel *

Department of Chemistry, Theory Center for Optical Science and Engineering, University of Rochester, P.O. RC Box 270216, Rochester, NY 14627-0216, USA

Received 7 November 2000

Abstract

Infrared photon echoes are simulated for an anharmonic vibrational dimer representing a dipeptide in the amide I spectral region by solving the nonlinear exciton equations for the vibrational-exciton model. New relaxation-induced resonances are predicted. Variations of the cross-peak intensities during the middle time interval show signatures of exciton population transfer and coherence dynamics. Enhanced resolution is achieved using phase sensitive detection. © 2001 Elsevier Science B.V. All rights reserved.

1. Introduction

Coherent multiple-pulse techniques are widely used in NMR to probe structure and dynamics of complex molecules [1]. Similar schemes proposed for the study of vibrational excitations using optical pulses [2–4] offer a new window into molecular structure with greatly improved (~100 fs) temporal resolution [2–4]. By controlling three time intervals (Fig. 1(A)), a heterodyne detected three-pulse measurement provides a three-dimensional (3D) projection of the system. Intervals t_1 and t_3 involve vibrational coherences whereas vibrational relaxation take place during the middle delay period t_2. Four distinct coherent two-dimensional (2D) techniques are possible when two of the pulses overlap temporally so that one of the delay times set to zero: photon echo, reverse photon echo, transient gratings, and reverse transient gratings [5]. The 2D vibrational response in proteins, polypeptides, liquids, and some model compounds have been shown to provide invaluable dynamical [2,6–10] and structural [11–16] information.

In this article we study the signatures of vibrational relaxation in 2D three-pulse IR spectra of the localized vibrational dynamics in the amide I spectral region. Implementation of different 2D IR vibrational PE techniques to study model $Rh(CO)_2$ compounds have been reported recently [17,18]. Advantages of the time and frequency resolved four wave mixing (Wigner spectrograms) were discussed in Refs. [19,20] and applications to photon echoes were presented in Refs. [21,22]. Spectrally resolved vibrational echoes, have been

* Corresponding author. Tel.: +1-716-275-3080; fax: +1-716-473-6889.

E-mail address: mukamel@chem.rochester.edu (S. Mukamel).

[1] Present address: Department of Chemistry, University of Wisconsin, Madison, WI 53706, USA.

[2] Present address: Corning Incorporated, Process Engineering and Modeling, Corning, NY 14831, USA.

0301-0104/01/$ - see front matter © 2001 Elsevier Science B.V. All rights reserved.
PII: S0301-0104(01)00231-2

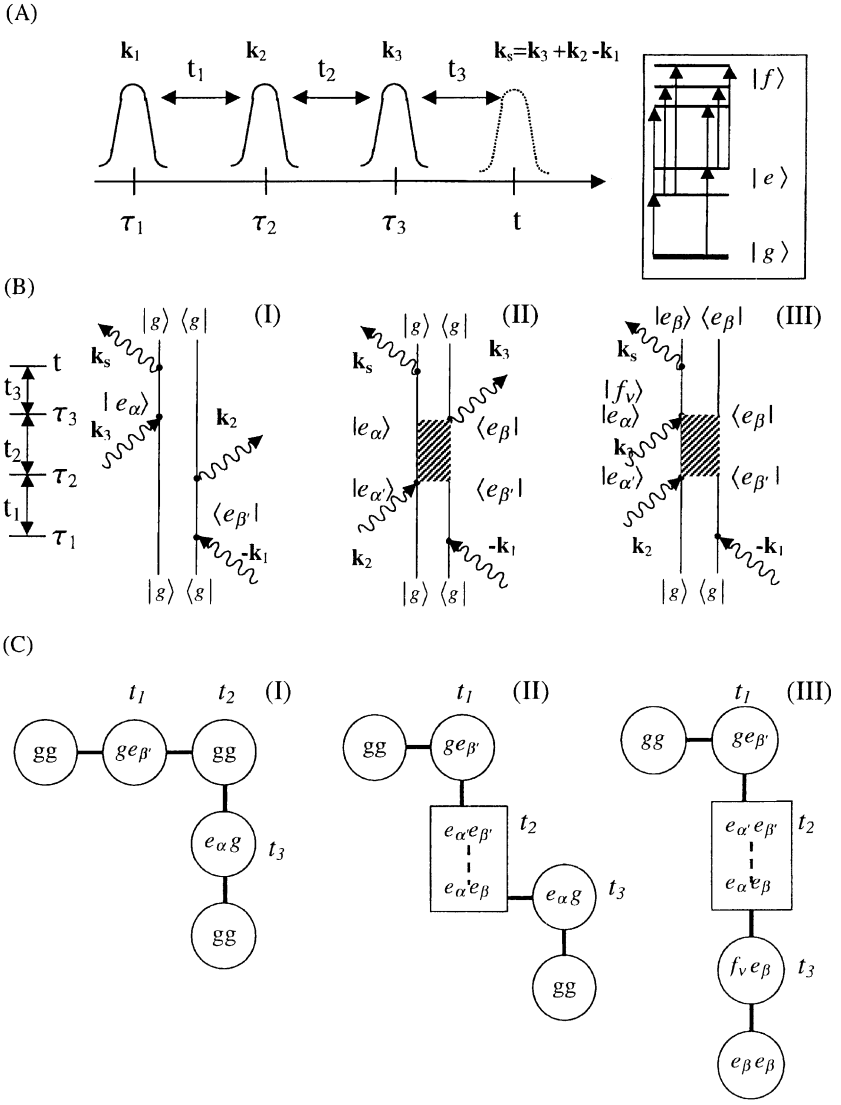

Fig. 1. (A) Pulse sequence in a three-pulse heterodyne technique involving optical transitions between the ground, one- and two-exciton manifolds shown in the insert. The PE signal is generated in the direction $\mathbf{k}_s = \mathbf{k}_3 + \mathbf{k}_2 - \mathbf{k}_1$. (B) The three Feynman diagrams describing all contributions to the PE signal for the three-level exciton system. (C) Liouville-space pathways associated with the various Feynman diagrams.

measured in N_3^- and HbCO [23]. Similar measurements of coupled C–O stretches in $Rh(CO)_2$ were reported in Ref. [17], and were compared with previous integrated IR PE studies [6]. Heterodyne detected time-resolved, Fourier transformed 2D PE spectra of the same system were presented in Ref. [18]. Vibrational anharmonicities and mode anharmonic coupling parameters were extracted from the 2D spectra. The absolute value, phase as well as the real and imaginary parts of the 2D vibrational photon echo signal for model glycine dipeptide and pentapeptide were computed [24,25]. Features of 2D PE spectra, recently measured using heterodyne detection technique from *N*-methyl-acetamide and acyl-proline-NH_2 [26] are in good agreement with the simulations. The 2D

PE signal during fast unfolding events in β-peptide following the T-jump were simulated in Refs. [14,15]. Most of these 2D studies, set $t_2 = 0$ and focused therefore on dephasing processes rather than vibrational-exciton relaxation. t_2 resolved spectra were reported in Ref. [23]. These measurements show spectral diffusion but not vibrational transfer since they were conducted on a single anharmonic vibrational mode of N_3^- and the CO stretch of HbCO.

In the present work we simulate the variation of the signal with t_2 for a vibrational dimer in the amide I spectral region. The dimer serves as a model system that shows all coherence and relaxation phenomena characteristics of larger peptides. The possible cross-peaks which carry information about vibrational couplings and their origin are introduced in Section 2. Section 3 presents simulations of the variation of the signal with t_2. Discussion and conclusions are given in Section 4.

2. Liouville-space pathways and cross-peaks for vibrational echoes

The eigenstates of coupled localized vibrations may be grouped into distinct manifolds according to the number of excitations. Starting with N three-level vibrational monomers, a three-pulse experiment only involves the ground state, a manifold of single excitations $|e_\alpha\rangle$ with energies ε_α, $\alpha = 1,\ldots,N$, and double excitations $|f_\nu\rangle$ with energies $\bar{\varepsilon}_\nu$, $\nu = 1,\ldots,N(N+1)/2$ (insert Fig. 1). We consider a vibrational three-pulse photon echo (3PE) experiment in which the vibrational-exciton system is excited by short infrared pulses separated by t_1 and t_2 delay times (Fig. 1(A)) with wave vectors $\mathbf{k}_1$, $\mathbf{k}_2$ and $\mathbf{k}_3$. Heterodyne detection of the induced polarization also controls the delay time t_3 after the third pulse. The 3PE signal [24,25] generated along the direction $\mathbf{k}_s = \mathbf{k}_3 + \mathbf{k}_2 - \mathbf{k}_1$ [5,27,28] is

$$S(\Omega_3,\Omega_1;t_2) = \int_0^\infty \mathrm{d}t_1 \int_0^\infty \mathrm{d}t_3 \exp(\mathrm{i}\Omega_1 t_1 + \mathrm{i}\Omega_3 t_3) \times R^{(3)}(t_3,t_2,t_1) \qquad (2.1)$$

Here $R^{(3)}(t_3,t_2,t_1)$ is the third-order nonlinear response function which for the vibrational Frenkel exciton model [29,30] depends on the one- and two-exciton manifolds [7,24,25]. It can be expressed in terms of one-exciton Green function, exciton scattering matrix and the exciton population Green functions [27]. Assuming linear coupling between the excitons and harmonic bath degrees of freedom, these quantities may be obtained by solving a closed set of equations for the one-exciton coherence, one–two-exciton coherence and exciton density matrix, respectively, derived in Ref. [28] and referred as the nonlinear exciton equations (NEE). The calculations presented in this article employ closed expressions for the third order response function $R(t_3,t_2,t_1)$ (Eqs. (2.8), (A6) and (A10) of Ref. [5]) derived by solving the NEE equations. This approach offers tremendous numerical advantages over the more conventional sum over states expressions and its favorable size scaling makes it most suitable for large peptides [2,5,24,25,27,28].

The various contributions to the signal may be classified and visualized using the double-sided Feynman diagrams shown in Fig. 1(B). There are three diagrams (I), (II), and (III) each representing a distinct Liouville-space pathway [32] as shown in Fig. 1(C). Generally, the first pulse creates a one-exciton coherence (ρ_{ge}) which evolves during t_1. The t_3 period has one-exciton (ρ_{eg}) or two-exciton (ρ_{fe}) type coherences. The dynamics of the exciton density matrix which involves vibrational relaxation takes place during the t_2 interval are described by the Green function $\mathscr{G}_{\alpha\beta;\alpha'\beta'}(t_2)$ which is represented by shaded boxes in diagrams (II) and (III). These diagrams show the interplay of transport and correlations between the t_1 and t_3 coherence periods in the signal.

The calculations presented below assume two coupled three-level anharmonic vibrations with $\Omega_0 = 1677$ cm^{-1} 0–1 transition energies, anharmonicity $\Delta = -16$ cm^{-1} and 1–2 to 0–1 transition dipole ratios $\kappa = \sqrt{2}$. The dipole–dipole coupling is $J = 10$ cm^{-1} (We are using the notation of Refs. [5,24,25]). This model represents typical amide I vibrations, such as the glycine dipeptide [24,25]. Using these parameters, the exciton manifold [24,25] (Fig. 1 insert) consists of two one-exciton

Table 1
All possible 2D PE resonances of the vibrational dimer (see Fig. 2) associated with the Liouville-space pathways shown in Fig. 1(B)–(C)

Resonance	Pathways	(Ω_1,Ω_3)	cm^{-1}	Resonance	Pathways	(Ω_1,Ω_3)	cm^{-1}
1	I, II	$(-\varepsilon_1,\varepsilon_1)$	$(-1687,1687)$	1′	I, II	$(-\varepsilon_2,\varepsilon_2)$	$(-1667,1667)$
2	I, II	$(-\varepsilon_1,\varepsilon_2)$	$(-1687,1667)$	2′	I, II	$(-\varepsilon_2,\varepsilon_1)$	$(-1667,1687)$
3	III	$(-\varepsilon_1,\bar{\varepsilon}_1-\varepsilon_1)$	$(-1687,1681)$	3′	III	$(-\varepsilon_2,\bar{\varepsilon}_1-\varepsilon_2)$	$(-1667,1701)$
4	III	$(-\varepsilon_1,\bar{\varepsilon}_2-\varepsilon_1)$	$(-1687,1638)$	4′	III	$(-\varepsilon_2,\bar{\varepsilon}_2-\varepsilon_2)$	$(-1667,1658)$
5	III	$(-\varepsilon_1,\bar{\varepsilon}_3-\varepsilon_1)$	$(-1687,1651)$	5′	III	$(-\varepsilon_2,\bar{\varepsilon}_3-\varepsilon_2)$	$(-1667,1671)$
6	III	$(-\varepsilon_1,\bar{\varepsilon}_1-\varepsilon_2)$	$(-1687,1701)$	6′	III	$(-\varepsilon_2,\bar{\varepsilon}_1-\varepsilon_1)$	$(-1667,1681)$
7	III	$(-\varepsilon_1,\bar{\varepsilon}_2-\varepsilon_2)$	$(-1687,1658)$	7′	III	$(-\varepsilon_2,\bar{\varepsilon}_2-\varepsilon_1)$	$(-1667,1638)$
8	III	$(-\varepsilon_1,\bar{\varepsilon}_3-\varepsilon_2)$	$(-1687,1671)$	8′	III	$(-\varepsilon_2,\bar{\varepsilon}_3-\varepsilon_1)$	$(-1667,1651)$

states $|e\rangle$ with energies $\varepsilon_1 = 1687\ cm^{-1}$ and $\varepsilon_2 = 1667\ cm^{-1}$, and three two-exciton states $|f\rangle$ with energies $\bar{\varepsilon}_1 = 3368\ cm^{-1}$, $\bar{\varepsilon}_2 = 3325\ cm^{-1}$, and $\bar{\varepsilon}_3 = 3338\ cm^{-1}$.

Pathway (I) represents correlation between one-exciton coherences $\rho_{ge_{\beta'}}$ during t_1 and $\rho_{e_\alpha g}$ during t_3 giving rise to 2D resonances at $(-\varepsilon_{\beta'},\varepsilon_\alpha)$. These include diagonal peaks $(\alpha=\beta')$ and cross-peak $(\alpha\neq\beta')$. During t_2 the system is in the ground state ρ_{gg} and this pathway therefore contains no signatures of vibrational relaxation. Pathway (II) shows correlations between the same coherences as pathway (I) resulting in the same cross-peak pattern. However, during t_2 the system is in the one-exciton manifold, where the one-exciton density matrix evolves from $\rho_{e_{\alpha'}e_{\beta'}}$ to $\rho_{e_\alpha e_\beta}$, as described by $\mathscr{G}_{\alpha\beta;\alpha'\beta'}(t_2)$. Both pathways (I) and (II) only depend on the single-exciton manifold. The two-exciton $|f\rangle$ states only show up in (III). This pathway describes the correlation between one-exciton coherence $\rho_{ge_{\beta'}}$ during t_1 and one- to two-exciton coherences $\rho_{f_\nu e_\beta}$ during t_3, giving rise to the cross-peaks $(-\varepsilon_{\beta'},\bar{\varepsilon}_\nu-\varepsilon_\beta)$. Like pathway (II), the system is in the excited state during t_2 where the density matrix evolves from $\rho_{e_{\alpha'}e_{\beta'}}$ to $\rho_{e_\alpha e_\beta}$, as represented by $\mathscr{G}_{\alpha\beta;\alpha'\beta'}(t_2)$. It is important to note that in the absence of vibrational relaxation during t_2 (i.e. $\alpha'=\alpha$ and $\beta'=\beta$), only $(-\varepsilon_\beta,\bar{\varepsilon}_\nu-\varepsilon_\beta)$ cross-peaks can be observed in addition to the one-exciton resonances. The cross-peaks $(-\varepsilon_{\beta'},\bar{\varepsilon}_\nu-\varepsilon_\beta)$, with $\beta\neq\beta'$ are particularly interesting, since they are induced by vibrational relaxation.

The sixteen possible peaks in the 2D spectra and the corresponding diagrams are summarized in Table 1. Resonances 1′–8′ are obtained from 1–8 by simply interchanging ε_1 and ε_2. The resonances 1, 2, 1′, 2′ reflect one-exciton correlations (pathways (I) and (II)) whereas 3–8 and 3′–8′ show one-two-exciton correlations (pathway (III)). The cross-peaks 3–5 and 3′–5′ exist even in the absence of vibrational relaxation [20] whereas peaks 6–8 and 6′–8′ are induced by vibrational relaxation and vanish when the coupling to the bath is switched off.

The left column of Fig. 2 shows the calculated absolute value of the 2D PE signal for various values of t_2 between 0.0 and 2.0 ps. A small homogeneous dephasing rate (which determines the width of the various resonances) was used. Most possible resonances are clearly resolved and marked in the $t_2 = 0$ ps and $t_2 = 2.0$ ps panels. The 1–8 resonances lie in the $\Omega_1 = -\varepsilon_1$ slice of the 2D spectrum whereas 1′–8′ show up in the $\Omega_1 = -\varepsilon_2$ slice. These resonances are only partially resolved in the right column which uses a larger homogeneous dephasing rate. Inhomogeneous broadening which may result in additional spectral features [24,25] was not included in these simulations. In Section 3 we analyze the t_2 variation of the signal, which provides a direct probe for exciton dynamics.

3. Two-dimensional spectroscopic signatures of exciton dynamics

The dynamics of the exciton density matrix $\rho_{e_\alpha,e_\beta}(t)$ during t_2 is described by the Redfield equations

$$\frac{d\rho_{e_\alpha,e_\beta}}{dt} = -i\omega_{\alpha\beta}\rho_{e_\alpha,e_\beta} + \sum_{\alpha'\beta'} R_{\alpha\beta;\alpha'\beta'}\rho_{e_{\alpha'},e_{\beta'}} \tag{3.1}$$

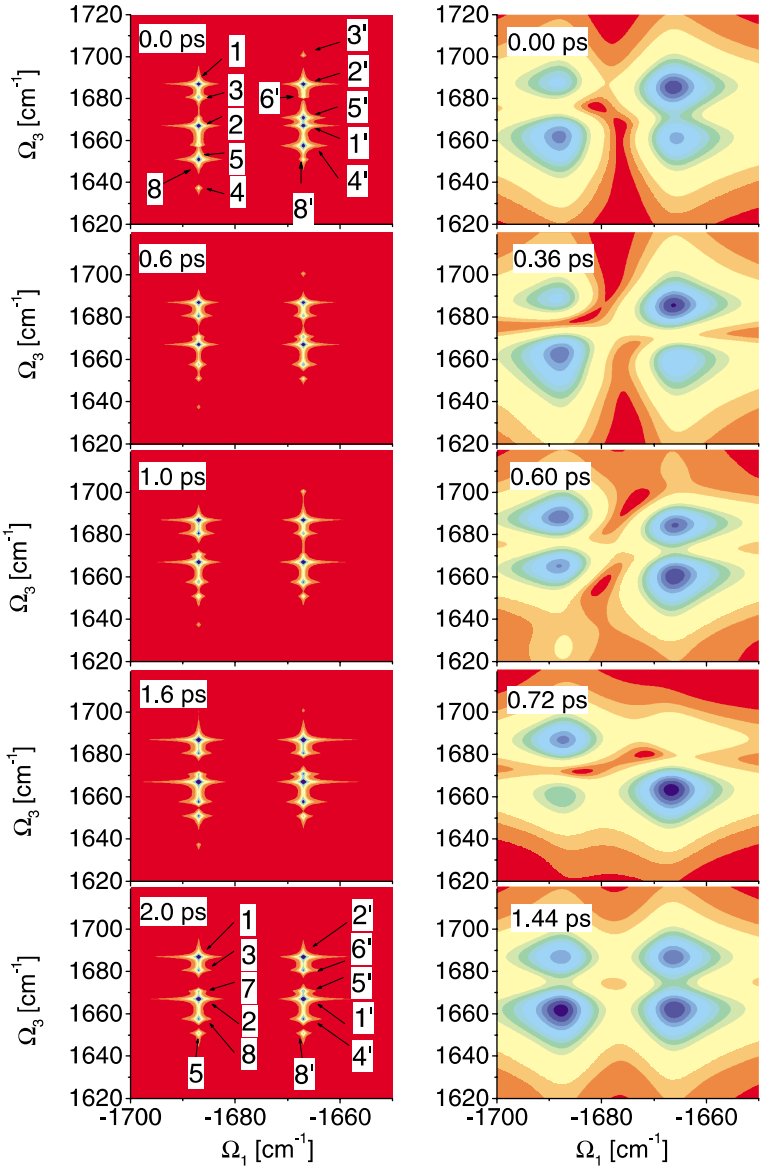

Fig. 2. Computed 2D PE signal for two sets of homogeneous dephasing rates which determine width of the (Ω_1, Ω_3)-resonances. The population decay rate $\gamma = 0.2$ cm^{-1}. Left column: small homogeneous dephasing rate of the first excited state with respect to the ground state of a monomeric unit $\Gamma = 0.2$ cm^{-1}, and doubly excited state with respect to the ground state $\gamma^{(2)} = 0.4$ cm^{-1}. Right column: Large homogeneous dephasing rates $\Gamma = 5$ cm^{-1} and $\gamma^{(2)} = 10$ cm^{-1} [7,11].

where $R_{\alpha\beta;\alpha'\beta'}$ is the Redfield relaxation superoperator $\omega_{\alpha\beta} = \varepsilon_\alpha - \varepsilon_\beta + 2i\gamma$, and γ is the one-exciton population decay rate. The Redfield tensor was calculated at room temperature ($k_B T = 200$ cm^{-1}). We used the overdamped Brownian oscillator spectral density to model the coupling with the bath, assuming that each peptide group is coupled to its own uncorrelated bath [32] setting the exciton-bath coupling energy to $\lambda = 1$ cm^{-1} and the bath relaxation width to $\Lambda = 100$ cm^{-1}. Expressions for the Redfield tensor in terms of the bath spectral density and one-exciton Green

functions are given in Eqs. (C14)–(C15) of Ref. [31]. The solution to Eq. (3.1) can be represented in terms of the Green function $\rho_{e_\alpha,e_\beta}(t) = \sum_{\alpha'\beta'} \mathscr{G}_{\alpha\beta;\alpha'\beta'}(t)\rho_{e_{\alpha'},e_{\beta'}}(0)$ [3] which controls the 2D PE signal during t_2 [5,28]. This Green function was computed by expanding it in the eigenvectors of the Redfield superoperator and transforming back to the exciton basis set [31,33]. The exciton scattering matrix was calculated using Eqs. (A3)–(A5) of Ref. [5], followed by calculation of the exciton Green function and the numerical integration of Eqs. (A6) and (A10) of Ref. [5].

In the present model, the 4×4 Redfield superoperator (and the Green function) acting on the single-exciton manifold are partitioned into a population block (connecting 11 and 22 density matrix elements) and a coherence block (connecting the 12 and 21 elements). Cross-elements between these blocks vanish due to dimer symmetry. The population eigenvalues are $\lambda_1 = -0.2$ cm^{-1} representing population decay rate, $\lambda_2 = -7.9$ cm^{-1} population relaxation rate within the one-exciton manifold. The Redfield Green function has the elements: $\mathscr{G}_{11,11}(t_2)$ and $\mathscr{G}_{22,22}(t_2)$, describing biexponential population decrease with T_1 and population decay time $\tau \equiv -2\pi/\lambda_1 = 27$ ps, as well as $\mathscr{G}_{11,22}(t_2)$ and $\mathscr{G}_{22,11}(t_2)$ describing population transfer between the exciton states (T_1) and population decay (τ). The eigenvalues of the coherent block are $\lambda_{3,4} = -4.0 \pm 20.4\mathrm{i}$ cm^{-1}. The imaginary part is the one-exciton energy splitting renormalized by the coupling to the bath, and the real part is the dephasing rate. These represent the elements $\mathscr{G}_{12,12}(t_2)$, $\mathscr{G}_{21,21}(t_2)$, $\mathscr{G}_{21,12}(t_2)$, and $\mathscr{G}_{12,21}(t_2)$, which describe the dynamics of coherences between the one-exciton states which oscillate with period $T = -2\pi/\mathrm{Im}(\lambda_{3,4}) = 1.6$ ps, dephasing (T_2) and decay (τ). We define the population relaxation time $T_1 \equiv -1/\lambda_2 = 0.7$ ps and the dephasing time $T_2 \equiv -1/\mathrm{Re}(\lambda_{3,4}) = 1.4$ ps. They satisfy $2T_1 = T_2$, indicating the absence of pure dephasing in the present simulations.

The evolution of the signal during t_2, is shown in Fig. 2. The increase of the intensities of 7, 8, 6′, 8′ peaks with t_2 reflects exciton population relaxation. This is more clearly seen in Fig. 3 which displays the $\Omega_1 = -\varepsilon_1$ (upper panel) and $\Omega_1 = -\varepsilon_2$ (lower panel) slices of Fig. 2 at different values of t_2. For $t_2 = 0$ ps the former ($\Omega_1 = -\varepsilon_1$) is dominated by 1–3, 5, 6 resonances and the latter ($\Omega_1 = -\varepsilon_2$) by 1′, 2′, 5′, 6′. The weak cross-peaks 4, 6 and 3′, 7′ are not resolved. Population dynamics induces intensity redistribution between the cross-peaks and at $t_2 = 2.0$ ps both slices are very similar.

The time evolution of the absolute value, the real, and the imaginary parts of each peak is shown in Fig. 4. We note that the real part (panels (D) and (D′)) representing correlations between the one-exciton states is negative, whereas the real part of the cross-peaks in panels (E), (F), (E′), and (F′) representing correlations between the single and two-exciton states is positive. This sign difference which can be used to enhance the resolution of closely-lying resonances illustrates the

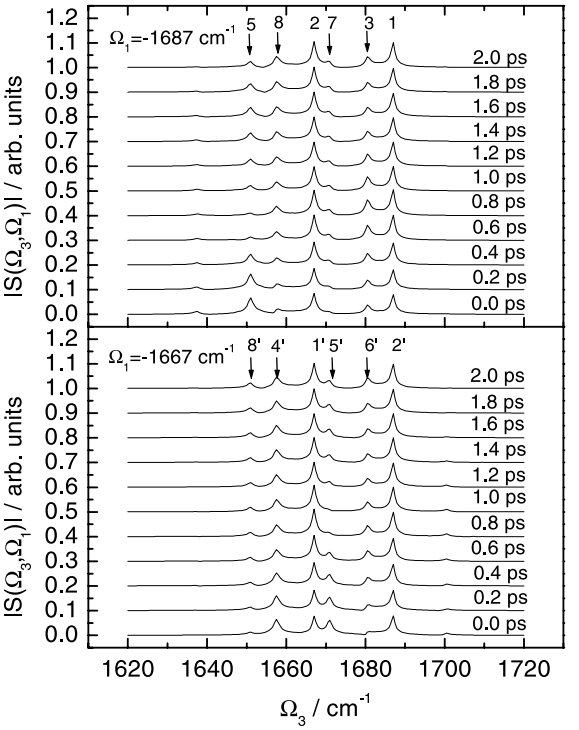

Fig. 3. Upper panel: $\Omega_1 = -\varepsilon_1$ slice, and lower panel: $\Omega_1 = -\varepsilon_2$ slice of the 2D PE signal of Fig. 2 (left column), calculated for different t_2 delay times.

[3] In Refs. [5,28] $\rho_{e_\alpha,e_\beta}(t)$ and $\mathscr{G}_{\alpha\beta,\alpha'\beta'}(t)$ were denoted by $N_{\alpha\beta}(t)$ and $G^{(N)}_{\alpha\beta,\alpha'\beta'}(t)$, respectively.

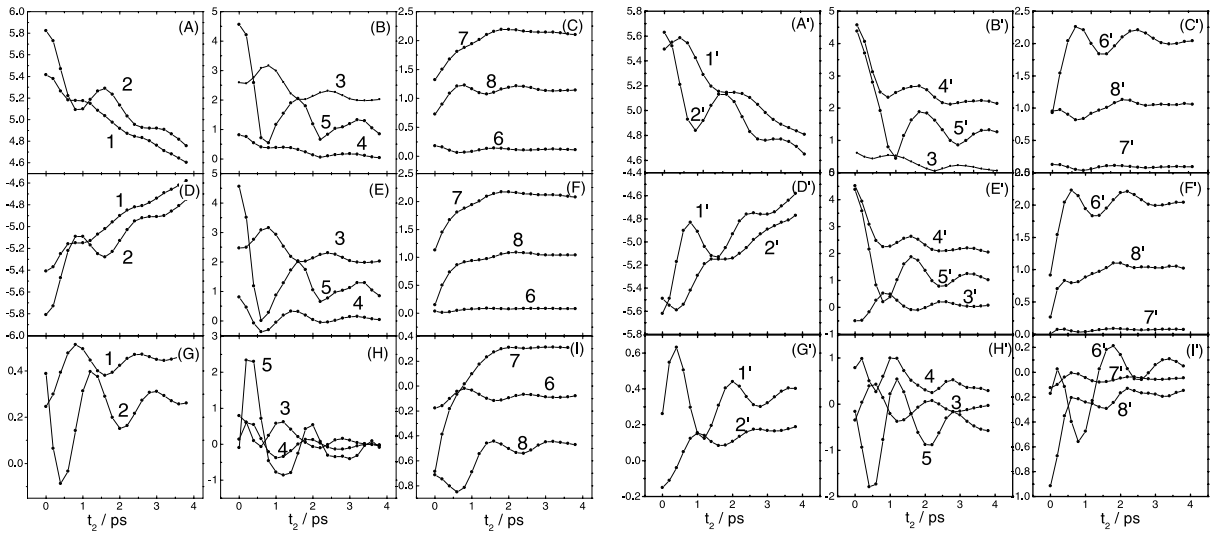

Fig. 4. Time evolution of the 2D PE resonances (Table 1) in Fig. 2 (left column). Upper row – absolute value; middle row – real part; bottom row – imaginary part of the signal.

usefulness of phase sensitive detection which probes the real and the imaginary parts of the signal. Since, T_1 and T_2 are comparable, the evolution reflects both of the population and coherence block of the exciton density matrix. The latter shows up as oscillations and the former as increase or decrease in the averaged amplitude of the signal. Coherent oscillations may also be used to improve the resolution of congested spectra. By a proper choice of t_2, the relative amplitudes of strongly overlapping cross-peaks can be varied and controlled. The signal oscillations are more pronounced for the real and imaginary parts, as can be seen in panels (H), (I), (H′), and (I′). The cross-peak imaginary parts change their sign during the oscillations, further enhancing the resolution.

The contributions of the coherent and incoherent blocks of the Green function to Fig. 4 are plotted separately in Figs. 5 and 6. Note that the total signal in Fig. 4(A)–(C), (A′)–(C′) is not simply a sum of Figs. 5 and 6 since it represents the absolute value of the superposition of two complex amplitudes.

The signal computed with the coherent block of $\mathscr{G}$ is shown in Fig. 5. According to pathways (II) and (III) (Fig. 1(B)–(C)), the diagonal 1 and cross-peaks 6–8 (1′ and 6′–8′) are proportional to $\mathscr{G}_{21,12}(t_2)$ ($\mathscr{G}_{12,21}(t_2)$). Variation of the cross-peaks 2 and 3–5 (2′ and 3′–5′) are determined by $\mathscr{G}_{21,21}(t_2)$ ($\mathscr{G}_{12,12}(t_2)$). The signal oscillates with frequency associated with the energy difference between the one-exciton states and its multiples. For the resonances 1, 5, 3, 1′, 3′, 5′, the real and imaginary parts of the signal oscillate harmonically with a $\sim\pi/2$ phase-shift, corresponding to vanishing oscillation amplitude of the absolute value as seen in the plot. The amplitude decays on the T_2 timescale, since $T_2 \ll \tau$.

Fig. 6 displays the contribution of the population block. According to pathways (II) and (III) (Fig. 1(B)–(C)), the absolute values of the resonances 1, 3–5 (1′, 3′–5′) are proportional to $\mathscr{G}_{11,11}(t_2)$ ($\mathscr{G}_{22,22}(t_2)$) and show biexponential decrease described by the T_1, since $T_1 \ll \tau$. The steep decrease of curves 1, 3–5 and 1′, 3′–5′ during the first picosecond corresponds to T_1, and the slow decay is τ. The cross-peaks 2, 6–8 (2′, 6′–8′) are proportional to $\mathscr{G}_{11,22}(t_2)$ ($\mathscr{G}_{22,11}(t_2)$). Their dynamics is determined by two competing processes, intensity increase on the T_1 timescale associated with vibrational relaxation between one-exciton states and decay on the τ timescale. The latter is dominating cross-peak 2. For cross-peak 2′

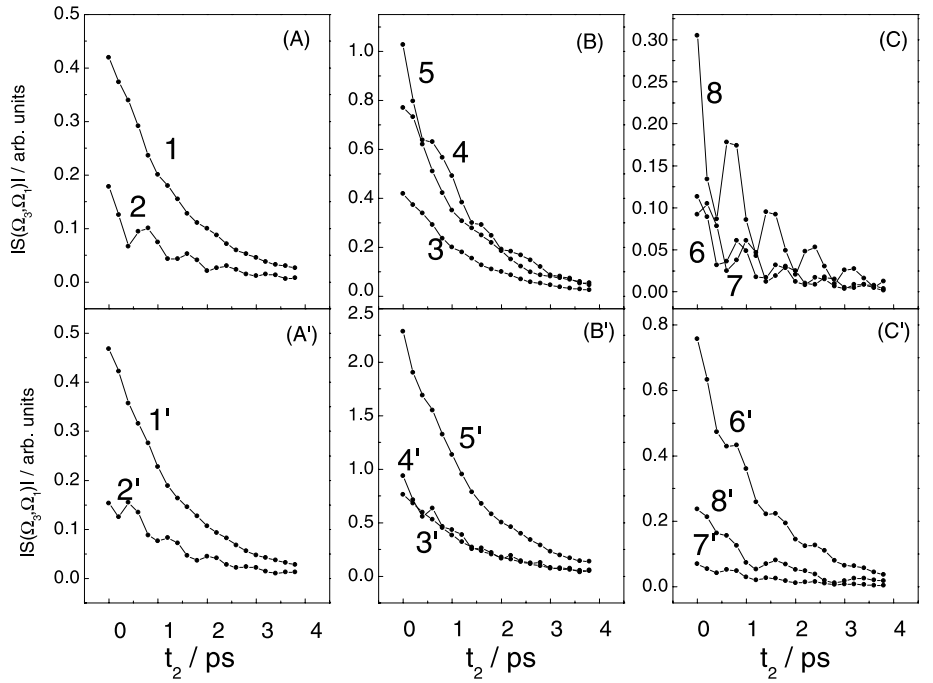

Fig. 5. The contribution of the coherence block of the exciton Green function $\mathcal{G}(t_2)$ to the absolute value of the 2D PE resonances.

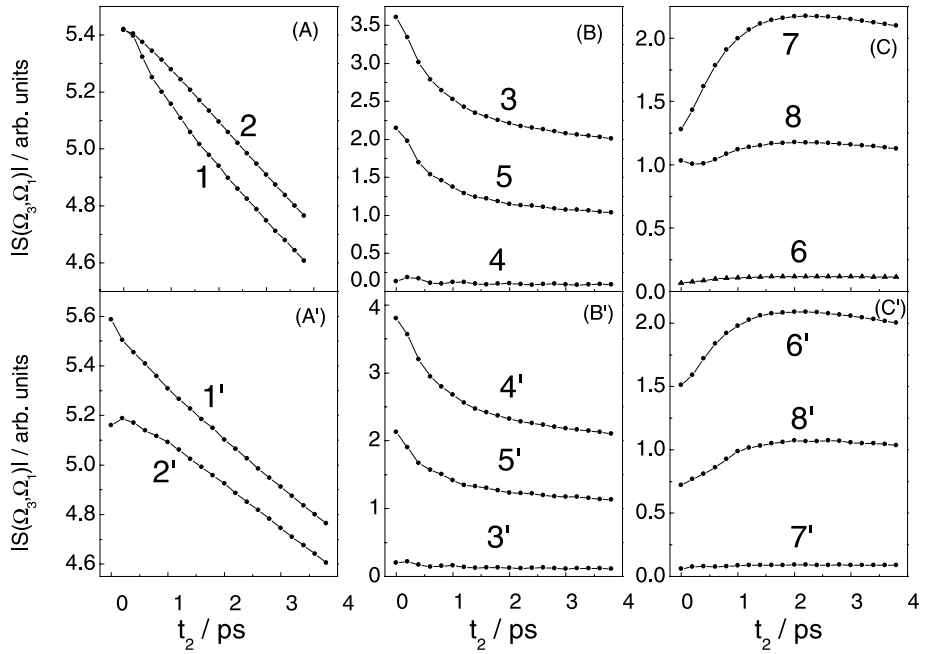

Fig. 6. The contribution of the population block of the exciton Green function $\mathcal{G}(t_2)$ to the absolute value of the 2D PE resonances.

population transfer shows up as a maximum at ~0.2 ps, and it is clearly seen for cross-peaks 6–8 and 6′–8′. On longer timescales when one-exciton states are thermalized, the intensity ratios for the resonances 1–8 and 1′–8′, respectively, is given by the Boltzmann factor times the ratio of the relevant oscillator strengths.

In the present simulations shown in Fig. 4 populations and coherences evolve on the same time scale. When pure dephasing is included their time scales may be very different, and the analysis of 2D spectra will be simplified. Fig. 5 should show coherent t_2 evolution of the resonant amplitudes dominated by the dephasing dynamics. (t_2 scale would change to subpicosecond range.) Signal controlled by population dynamics should resemble Fig. 6. Pure dephasing between the one-exciton states should be accompanied by pure dephasing between the one-exciton states and the ground state, resulting in the increase in the linewidth of the 2D resonances.

The right panel in Fig. 2 presents calculations with a larger homogeneous dephasing rate. The resonances of the left column now overlap and are only partially resolved. At $t_2 = 0$ ps we see four resolved peaks located around $(-1687, 1687)$, $(-1687, 1660)$, $(-1667, 1687)$, and $(-1667, 1687)$ whose intensities vary within $0.0 < t_2 < 0.36$ ps time interval. Significant changes in the spectrum occur during $0.54 < t_2 < 0.90$ ps due to coherence oscillations. At $t_2 \sim 0.60$ ps additional two cross-peaks around $(-1687, 1630)$ and $(-1667, 1710)$ show up and later vanish. These are the $(-\varepsilon_1, \bar{\varepsilon}_3 - \varepsilon_1)$ and $(-\varepsilon_2, \bar{\varepsilon}_3 - \varepsilon_2)$ resonances. This demonstrates how coherent oscillations can be used to resolve overlapping 2D resonances. The intensity redistribution between the $(-1687, 1687)$, $(-1687, 1660)$, $(-1667, 1687)$, and $(-1667, 1687)$ peaks reflects vibrational relaxation.

4. Discussion

Variation of the 2D 3PE signal during t_2 provides a direct probe for the Green function components $\mathscr{G}_{\alpha\beta,\alpha'\beta'}(t_2)$. For instance, $\mathscr{G}_{11,11}(t_2)$ and $\mathscr{G}_{11,22}(t_2)$ select different Liouville-space pathways and induce different resonances, namely 1 and 2′, respectively as well as 3–5 and 6′–8′, respectively. Population relaxation parameters can thus be measured in impulsive experiments regardless of which exciton population is created by the pulses. Even for equally populated one-exciton states $\mathscr{G}_{11,11}(t_2)$ and $\mathscr{G}_{11,22}(t_2)$ should vary in time to compensate their contributions to $\rho_{e_1e_1}(t_2)$, and the variation should be seen as t_2 evolution of different cross-peaks. Since the population transfer rate determined by the Green function components does not vanish at $t_2 = 0$, new 7–8 and 6′, 8′ cross-peaks are observed in Fig. 2 at $t_2 = 0.0$ ps. The same argument can be made regarding the coherences. Anisotropy measurements may be used to probe $\rho_{e_\alpha,e_\beta}(t_2)$, i.e. actual changes in the exciton level populations. In this case the 2D spectrum at $t_2 = 0$ should contain only 1–5 and 1′–5′ resonances and the cross-peaks 6–8 and 6′–8′ should rise with increasing t_2, following changes of the exciton population.

In previous studies of 2D 3PE [5,24,25] coherent dynamics was assumed during t_2 by factorizing the Green function $\mathscr{G}_{\alpha,\beta;\alpha',\beta'}(t_2) = \delta_{\alpha,\alpha'}\delta_{\beta,\beta'}G_\alpha(t_2)G^\dagger_\beta(t_2)$, where G_α is one-exciton Green function in the exciton basis set. This factorization reduces the number of Liouville-space pathways and the cross-peaks $(-\varepsilon_\alpha, \bar{\varepsilon}_v - \varepsilon_\beta)$, $\alpha \neq \beta$ (i.e. 6–8 and 6′–8′ for the dimer) should vanish. The coherent oscillations of the 6–8 and 6′–8′ cross-peaks observed in the present simulations reflect the $\mathscr{G}_{12,21}$ and $\mathscr{G}_{21,12}$ elements of the Green function, induced by the coupling to the bath. They correspond to the vibrational energy redistribution in the coherence block of the Redfield equation.

Anisotropy measurements of 2D IR PE vs. t_2 should provide information on the exciton energy spatial redistribution within certain protein secondary structure motif, such as α-helix. The cross-peak intensities should be proportional to the dipole moment projections of the coupled groups. Different fragments of a protein may have different local environments which may lead to different population relaxation rates. In this case t_2 delayed measurements should be able to probe couplings between amide group which belong to particular local structure. In addition coherent t_2 oscillations of the signal may be employed to resolve strongly-congested resonances.

In summary, we have demonstrated the signatures of vibrational relaxation in the 2D 3PE technique. Simulations performed for the anharmonic vibrational dimer in the amide I spectral region show new cross-peaks induced by population transfer within the one-exciton manifold. Population relaxation, population decay and dephasing timescales can be determined from the t_2 evolution of the cross-peak amplitudes. Coherent oscillations of the signal can be used to improve the resolution of overlapping cross-peaks.

Acknowledgements

The support of the National Science Foundation and the Petroleum Research Fund administered by the American Chemical Society is gratefully acknowledged.

References

[1] R.R. Ernst, G. Bodenhausen, A. Wokaun, Principles of Nuclear Magnetic Resonance in One and Two Dimensions, Clarendon Press, Oxford, 1987.
[2] Y. Tanimura, S. Mukamel, J. Chem. Phys. 99 (1993) 9496.
[3] S. Mukamel, Ann. Rev. Phys. Chem. 51 (2000) 691.
[4] S. Mukamel, A. Piryatinski, V. Chernyak, Acc. Chem. Res. 32 (1999)145.
[5] W.M. Zhang, V. Chernyak, S. Mukamel, J. Chem. Phys. 110 (1999) 5011.
[6] K.D. Rector, A.S. Kwok, C. Ferrante, A. Tokmakoff, C.W. Rella, M. Fayer, J. Chem. Phys. 106 (1997) 10027.
[7] P. Hamm, M. Lim, R.M. Hochstrasser, J. Phys. Chem. B 102 (1998) 6123.
[8] P. Hamm, M. Lim, W.F. DeGrado, R.M. Hochstrasser, J. Phys. Chem. A 103 (1999) 10049.
[9] W. Zhao, J. Wright, Phys. Rev. Lett. 84 (2000) 1411.
[10] R.B. Williams, R. Loring, J. Chem. Phys.113 (2000) 1932.
[11] P. Hamm, M. Lim, W.F. DeGrado, R. Hochstrasser, Proc. Nat. Acad. Sci. 96 (1999) 2036.
[12] P. Hamm, M. Lim, W. DeGrado, R. Hochstrasser, J. Chem. Phys. 112 (2000) 1907.
[13] S. Woutersen, P. Hamm, J. Phys. Chem. 104 (2000) 11316.
[14] C. Scheurer, A. Piryatinski, S. Mukamel, in: T. Elsässer, S. Mukamel, M. Murnane, N.F. Scherer (Eds.), Ultrafast Phenomena XII, Springer Series in Chemical Physics, 2001, p. 507.
[15] C. Scheurer, A. Piryatinski, S. Mukamel, J. Am. Chem. Soc., in press.
[16] K. Okumura, A. Tokmakoff, Y. Tanimura, J. Chem. Phys. 111 (1999) 492.
[17] K.A. Merchant, D.E. Thompson, M.D. Fayer, Phys. Rev. Lett., submitted for publication.
[18] O. Golonzka, M. Khalil, N. Demirdoven, A. Tokmakoff, Phys. Rev. Lett., submitted for publication.
[19] S. Mukamel, C. Ciordas-Ciurdariv, V. Khidekel, IEEE J. Quant. Electron. 32 (1996) 1278.
[20] S. Mukamel, J. Chem. Phys. 107 (1997) 4165.
[21] T. Meier, V. Chernyak, S. Mukamel, J. Chem. Phys. 107 (1997) 8759.
[22] S. Yokojima, T. Meier, V. Chernyak, S. Mukamel, Phys. Rev. B 59 (1999) 12584.
[23] M.C. Asplund, M. Lim, R.M. Hochstrasser, Chem. Phys. Lett. 323 (2000) 269.
[24] A. Piryatinski, S. Tretiak, V. Chernyak, S. Mukamel, J. Raman Spectrosc. 31 (2000) 125.
[25] A. Piryatinski, V. Chernyak, S. Mukamel, in: M.D. Fayer (Ed.), Ultrafast Infrared and Raman Spectroscopy, Marcel Dekker, New York, 2001, pp. 349–382.
[26] M.C. Asplund, M.T. Zanni, R. Hochstrasser, Proc. Nat. Acad. Sci. 97 (2000) 8219.
[27] V. Chernyak, N. Wang, S. Mukamel, Phys. Rep. 263 (1995) 213.
[28] V. Chernyak, W.M. Zhang, S. Mukamel, J. Chem. Phys. 109 (1998) 9587.
[29] S. Krimm, J. Bandeker, J. Adv. Protein Chem. 38 (1986) 181.
[30] H. Torii, M. Tasumi, J. Chem. Phys. 96 (1992) 3379.
[31] M. Dahlbom, T. Minami, V. Chernyak, T. Pullerits, V. Sundsreöm, S. Mukamel, J. Phys. Chem. B 104 (2000) 3976.
[32] S. Mukamel, Principles of Nonlinear Optical Spectroscopy, Oxford University Press, New York, 1995.
[33] V. Chernyak, T. Minami, S. Mukamel, J. Chem. Phys. 112 (2000) 7953.